A Moist Potential Vorticity Model for Mid-Latitude Mesoscale Convective Systems over the Land

Qiu Yang,[a] L. Ruby Leung,[a] Zhe Feng,[a] Xingchao Chen[b]

[a] *Atmospheric Sciences and Global Change Division, Pacific Northwest National Laboratory, Richland, Washington, USA*

[b] *Department of Meteorology and Atmospheric Science, and Center for Advanced Data Assimilation and Predictability Techniques, The Pennsylvania State University, PA, USA*

Corresponding author: Qiu Yang, qiu.yang@pnnl.gov

ABSTRACT: Mesoscale convective systems (MCSs) are observed to bring large amounts of rainfall and severe wind gusts to the mid-latitude land regions, having a significant impact on local weather and hydrologic cycle. Yet present-day weather forecast models face a huge challenge in accurately predicting MCS life cycle and the associated precipitation, highlighting an urgent need for a better understanding of the underlying mechanisms. From a theoretical perspective, a suitable model to capture realistic properties of MCSs and isolate bare-bone mechanisms for their initiation, intensification, and eastward propagation is still lacking. To simulate mid-latitude MCSs over the land, we develop a simple moist potential vorticity (PV) model that readily describes the interactions among PV perturbations, air moisture, and soil moisture. Multiple experiments with or without various environmental factors and external forcing are used to investigate their impact on MCS dynamics and mesoscale circulation vertical structures. The result shows that mechanic forcing can induce lower-level updraft and cooling, providing favorable conditions for MCS initiation. It also demonstrates a positive feedback among surface winds, evaporation rate, and air moisture for MCS intensification. Besides, both background surface westerlies and vertical westerly shear lead to favorable conditions for the eastward propagation of MCSs. Lastly, it highlights the crucial role of stratiform heating in shaping mesoscale circulation response. The model should serve as a useful tool for understanding fundamental mechanisms of MCS dynamics.

1. Introduction

A mesoscale convective system is a complex of thunderstorms that are organized on a scale over hundred kilometers, thus inducing a vast impact on local weather and hydrologic cycle in the mid-latitude land regions (Houze 2004; Feng et al. 2016). Convective storms such as MCSs lead to more than 20 billion dollar annual economic losses in the U.S. (Munich RE 2016). When compared with individual thunderstorms that only persist a few hours, a MCS typically lasts for more than a day and releases a massive amount of rainfall. The MCS precipitation account for more than 50% of total warm-season rainfall in the central U.S (Fritsch et al. 1986; Jiang et al. 2006; Haberlie and Ashley 2019; Feng et al. 2019). With larger rain areas and higher rainfall intensity than non-MCS events, MCSs are attributed to the majority of slow-rising and hybrid floods in the U.S. east of 100°W (Hu et al. 2021a). Early observational studies about MCSs can date back to 1970s (Houze 1975; Betts et al. 1976; Houze 1977), which typically focus on individual events over small-area regions. The recent decades have seen prosperous research activities about structures and mechanisms of MCSs over the globe, thanks to the rapid development of satellite measurement and radar detection. For example, by jointly using geostationary satellite infrared brightness temperature and precipitation feature characteristics, Feng et al. (2021) used a novel tracking methodology to construct a global long-term high-resolution MCS database. Song et al. (2021, 2022) conducted a self-organizing map analysis to identify four types of summertime MCS initiation environments and the crucial role of eastward propagating environments in supporting MCS initiation over the U.S. Great Plains. Chen et al. (2022b,a, 2021b) used 19-year satellite observations to examine the sequential roles of non-deep convection, deep convection, and MCS in precipitation-moisture interactions and concluded with findings that MCS becomes the major rainfall type in a moist environment.

Despite the much progress in the observation, it is a huge challenge for both general circulation models (GCMs) and cloud-resolving models (CRMs) to simulate MCSs, particularly over the mid-latitude land regions. In contrast to the tropical regions where thermodynamic controlling factors such as convection-water vapor-radiation feedback dominate the MCS mechanisms (Held et al. 1993; Bretherton et al. 2005; Wing et al. 2017), mid-latitude regions are also influenced by many dynamic controlling factors such as synoptic forcing (Maddox 1983; Anderson and Arritt 1998; Coniglio et al. 2004, 2010), sub-synoptic eastward-moving perturbations (Li and Smith 2010;

Tuttle and Davis 2013; Wang et al. 2011a,b; Pokharel et al. 2019) as well as soil moisture feedback (Hu et al. 2021b). Such a complex situation with multiple controlling factors explains why even state-of-the-art numerical simulations still present significant biases in simulating mid-latitude MCSs, particularly during the summertime when synoptic forcing is typically weak. For example, compared with the standard Energy Exascale Earth System Model (E3SM), the superparameterized model (SP-E3SM) shows a better skill in simulating MCS number and precipitation amount, diurnal cycle, propagation, and probability distribution of precipitation rate in both spring and summer, but still underestimates MCS precipitation amount in comparison with the observation (Lin et al. 2022). By undertaking a 13-year North American scale convection-permitting climate simulation, Prein et al. (2017a) concluded that this simulation captures the main characteristics of the observed MCSs, but significantly underestimates the MCS frequency in the central U.S. during late summer. These difficulties in simulating summertime MCSs in the central U.S. also contributes to the large uncertainty in projecting future climate under the global warming. Prein et al. (2017b) further ran another 13-year continental-scale convection-permitting climate simulation but in a future warming environment to investigate climate change effects on MCSs, and concluded that there will be 30-80% increases in total MCS precipitation volume, but the uncertainty is typically difficult to narrow down.

To further reduce those simulation biases and projection uncertainty, we need a better understanding of fundamental physical mechanisms underlying the MCS dynamics, including its initiation, intensification and upscale growth as well as eastward propagation. Fortunately, many encouraging progresses in the theoretical perspectives have been made in the past few decades, particularly for tropical MCSs. One of the well-known theoretical studies about squall lines, an elongated-line type of MCSs, is the RKW theory (Rotunno et al. 1988; Weisman and Rotunno 2004). The core concept of RKW theory is that a surface-based cold pool and environmental vertical wind shear can counter each other and affect squall lines positively. Mapes (1993) demonstrated that a heating source associated with MCSs causes upward displacement in the surrounding area through inviscid gravity wave dynamics, theoretically predicting that cloud clusters should be gregarious. Moncrieff and Green (1972); Betts et al. (1976); Moncrieff and Miller (1976); Moncrieff (1978, 1981, 1985, 1992) did a series of pioneering studies on the slantwise structure and transport properties of organized convection, expediting the development of the coherent structure parameterization

(MCSP) (Moncrieff et al. 2017; Moncrieff 2019; Chen et al. 2021a) for the physical and dynamical effects of organized convection that are missing from contemporary parameterization in GCMs. By using the horizontal vorticity equation in Moncrieff and Green (1972), Zhang (in press) further developed an analytical model for steady-sate squall lines and successfully described their organization, propagation, and properties under sheared environment. As for the interactions between MCSs and larger-scale circulation, Yang and Majda first developed a theoretical multi-scale model to quantify the upscale impact of MCSs on convectively coupled equatorial waves (Yang and Majda 2017, 2018, 2019), then diagnostically calculated the contributions of MCSs on large-scale kinetic and potential energy budgets (Brenowitz et al. 2018; Yang et al. 2019a), and eventually proposed a basic parameterization of the upscale impact for coarse-resolution GCMs (Yang et al. 2019b).

In contrast, it is more challenging to theoretically model mid-latitude MCSs over the land, due to the presence of the Coriolis force, strong synoptic forcing, and complex interactions with land moisture. Yang et al. (2021) developed a simple Lagrangian parcel model for the initiation of summertime MCSs over the central U.S., based on the basic features of rising parcels and the cold pool interaction mechanisms. Yang et al. (in press) further used this model to investigate the impact of global warming on MCS initiation and growth. Raymond and Jiang (1990) developed a potential vorticity (PV) model for long-lived MCSs through a self-sustained interaction mechanism between vertical motion and diabatic heating. In particular, it showed that diabatic heating contributes to the creation of a lower-tropospheric positive PV anomaly, which can interact with a sheared environment to induce further lifting of low-level air. Here we extend the PV model of Raymond and Jiang (1990) into a moist version by explicitly resolving the moisture exchange between the atmosphere and land soil, aiming at developing a suitable framework for modeling mid-latitude MCSs over the land.

The overall goal of this study is to develop a moist PV framework for modeling mid-latitude MCSs over the land and use it to understand salient mechanisms associated with initiation, intensification, propagation, and vertical structures of MCSs. This goal is achieved through the following four aspects: 1) extend the PV model of Raymond and Jiang (1990) into a moist version by incorporating the moisture exchange between the free troposphere and soil as well as their interactions with the mesoscale circulation, 2) discuss the mechanic and thermal factors in initiating and intensifying the MCSs, 3) investigate the effects of background surface wind, and vertical shear on MCS

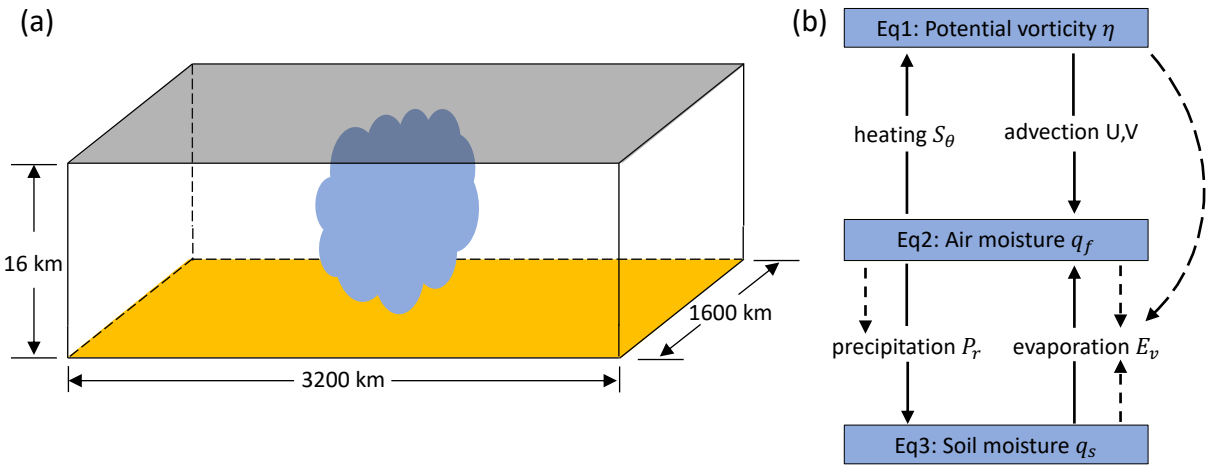

FIG. 1. (a) Schematic diagram for the model channel domain with a periodic boundary condition in the zonal direction and rigid boundary conditions in the meridional and vertical directions. It consists of a free troposphere model (white box above) for mesoscale circulation and air moisture, and a land surface model (yellow surface below) for soil moisture. (b) Interaction mechanisms among three components of the model (indicated by blue boxes), including PV, air moisture, and soil moisture. Solid arrows indicate the interaction forcing among these components, while dashed arrows indicate controlling factors in determining precipitation and evaporation.

propagation, 4) study the role of stratiform heating in determining the MCS dynamics and vertical structure.

The PV model of Raymond and Jiang (1990) includes a prognostic equation for a reduced PV perturbation variable, accounting for the mesoscale circulation associated with MCSs driven by diabatic heating, mechanic forcing, as well as advection effect. Here we further extend this dry model to a moist version by incorporating moisture budget equations in both the free atmosphere and soil. The new model readily describes the dominant mesoscale circulation and moisture exchange during the MCS life cycle over a mid-latitude land region (see Fig. 1a). Two physics-based schemes are used to parameterize precipitation and evaporation processes, mimicking the moisture exchange tendency between the free atmosphere and soil. The detailed road map for the interaction mechanisms among the PV perturbation, air moisture, and soil moisture is indicated in Fig. 1b. Besides, the model is configured with realistic environmental profiles based on air moisture, soil moisture, and vertical wind shear from observational and reanalysis data. For the sake of simplicity, the diabatic heating that results from latent heat release is chosen to be in a fixed

vertical profile under the guidance of cloud-resolving simulations. Finally, we consider multiple different scenarios to highlight the crucial role of several environmental factors and external forcing that could potentially affect the initiation, intensification, and propagation of MCSs. The result shows that external mechanic forcing induces low-level updraft and provides favorable conditions in initiating MCSs, while the evaporation-convection interaction promotes their further intensification. Besides the advection effect of background westerly flows, the eastward propagation of MCSs can be also induced by the asymmetric evaporation rate in the presence of surface westerlies as well as background westerly vertical shear. It also demonstrates the significant role of stratiform heating in affecting the mesoscale circulation associated with MCSs.

The rest of the paper is organized as follows. Section 2 summarizes the key properties of the model, numerical details and simulation setup, and input data from observational and reanalysis data. Section 3 discusses mechanic and thermal factors in initiating and intensifying MCSs, while section 4 focus on the effects of background surface wind and vertical shear on MCS propagation. Section 5 further investigates the role of stratiform heating on mesoscale circulation associated with MCSs. The paper concludes with a discussion in section 6. The derivation of this moist PV model is included in the appendix.

2. Methodology

In this section, we first briefly describe the derivation and key properties of the moist PV model for mid-latitude MCSs over the land. Then we summarize the numerical schemes for solving the model, and the setup details of all simulations that are used in this study. Finally, we document the data sources for environmental wind and moisture fields as input data in the model simulations.

a. A simple moist model for mid-latitude MCSs over the land

This simple model readily describes the mesoscale circulation and air-soil moisture exchange associated with MCSs over a mid-latitude land region (see Fig. 1a). It consists of three prognostic equations, which govern the dynamics of the reduced PV perturbation, air moisture, and soil moisture, respectively. A detailed description about each equation is summarized below.

The first equation (the first row in Table 1) for the reduced PV perturbation describes the mesoscale circulation associated with the MCSs, whose derivation follows Raymond and Jiang

TABLE 1. Governing equations in this simple moist model for mid-latitude MCSs over the land. The model resolves three prognostic variables, including reduced potential vorticity perturbation η, air moisture q_f, and soil moisture q_s. Both stream function ψ and pressure perturbation ϕ are inferred from η through PV inversion. Then buoyancy b is obtained through the hydrostatic balance equation $\frac{\partial \phi}{\partial z} = b$. Vertical velocity w is further induced diagnostically by using the buoyancy budget equation $\frac{\partial b}{\partial t} - \psi_y b_x + \psi_x b_y + N^2 w = \frac{g}{\tilde{\theta}} S_\theta$. In general, horizontal velocity can be represented as the sum of solenoidal and irrotational parts as $u = -\frac{\partial \psi}{\partial y} - \frac{\partial \zeta}{\partial x}, v = \frac{\partial \psi}{\partial x} - \frac{\partial \zeta}{\partial y}$, where ζ is velocity potential satisfying the divergence-free condition $\Delta\zeta = \frac{\partial w}{\partial z}$. $\Psi_1(z)$ is the fixed vertical profile of environmental air moisture. The notation $[\cdot] = \int_0^{H_z} \cdot dz$ means column integration from surface to the tropopause. S_θ, F_m, P_r, E_v stand for diabatic heating, mechanic forcing, precipitation, and evaporation, respectively. $\overrightarrow{\xi}_a = \left(-\psi_{xz}, -\psi_{yz}, \Delta\psi + f\right)$ is absolute vorticity. All variables with a tilde represent environmental profiles, including air density $\tilde{\rho}$, potential temperature $\tilde{\theta}$, potential vorticity $\tilde{q}$. Details about physical constant, parameters and the parameterized forcing are included in Table 2.

Component	Variable	Equations	Description
Reduced potential vorticity perturbation	η	$\eta_t - \psi_y \eta_x + \psi_x \eta_y = \frac{1}{\tilde{\rho}} \left[\nabla \cdot \left(S_\theta \overrightarrow{\xi}_a \right) - f \frac{\tilde{q}_z}{\tilde{q}} S_\theta \right] - \frac{1}{\tau} \eta + F_m$	PV thermal forcing S_θ, mechanical forcing F_m, and damping $-\frac{1}{\tau}\eta$
	$\eta \leftrightarrow \psi, \phi$	$\frac{f^2}{\tilde{\theta}\tilde{q}} \eta = \frac{f^2 \tilde{q}}{\tilde{\theta}^2 N^2} \left(\frac{\tilde{\theta}}{\tilde{q}} \phi_z \right)_z + \frac{f}{\tilde{\theta}} \Delta\psi - \frac{f}{N^2 \tilde{\theta}} \left(\psi_{xz} \phi_{xz} + \psi_{yz} \phi_{yz} \right)$ $\Delta \left(\phi - f\psi \right) = 2\psi_{xx}\psi_{yy} - 2\left(\psi_{xy}\right)^2$	PV inversion
Air moisture	q_f	$\left(q_f\right)_t + \left(\left[u \Psi_1(z) \right] q_f \right)_x + \left(\left[v \Psi_1(z) \right] q_f \right)_y = -P_r + E_v$	Column water vapor budget in the free atmosphere
Soil moisture	q_s	$\left(q_s\right)_t = P_r - E_v$	Soil moisture budget

(1990) (see Appendix a). To slightly simplify the final form of the equation, we choose to start with the hydrostatic primitive equations in the anelastic approximation so that the factor $\theta_0(z)$ in Eqs. 1-4 of Raymond and Jiang (1990) is absorbed into the geopotential variable in Eqs. A1-A5. In brief, the local time tendency of PV perturbation, η_t, is balanced by the 2-D advection term, $-\psi_y \eta_x + \psi_x \eta_y$, the term involving adiabatic heating, $\frac{1}{\tilde{\rho}} \left[\nabla \cdot \left(S_\theta \overrightarrow{\xi}_a \right) - f \frac{\tilde{q}_z}{\tilde{q}} S_\theta \right]$, atmospheric drag term, $-\frac{1}{\tau}\eta$, and mechanic forcing term, F_m. To invert streamfunction, ψ, and geopotential, ϕ, from the PV perturbation, η, this PV equation is accompanied by a par of two diagnostic equations (the second and third rows in Table 1). Without the last two nonlinear terms involving ψ and ϕ, these two diagnostic equations are reduced to the quasi-geostrophic case.

The second equation (the fourth row in Table 1) governs the column water vapor budget in the free atmosphere. Its derivation starts with the specific humidity budget equation in a flux form and

TABLE 2. Physical constant and parameters, the parameterized forcing, and numerical details in the model.

Category	Symbol	Value	Description
Constant	f	$9.3745 \times 10^{-5}\ rad/s$	Coriolis frequency at latitude 40 deg N
	g	$9.81\ m/s^2$	gravity acceleration
	L_v	$2.26 \times 10^3\ kJ/kg$	specific latent heat for condensation of water vapor
	ρ_w	$1.0 \times 10^3\ kg/m^3$	liquid water density
	C_p	$1.0\ kJ/kg/K$	specific heat capacity of air
Parameter	τ	$1\ day$	PV damping time scale due to momentum friction
	$q_{f,0}$	$35.11\ mm$	environmental column water vapor
	$q_{s,0}$	$102.0\ mm$	environmental soil moisture
Forcing	P_r	$a_0 e^{b_0(q_f - q_{f,0})} + c_0$	surface precipitation rate (dimensionless), coefficient values $a_0 = 0.123$, $b_0 = 1.20$, $c_0 = 0.052$ are obtained by fitting ERA5 reanalysis and WRF simulation data
	S_θ	$\frac{1}{\alpha}(P_r - P_{r,0})\Psi_2(z)$	diabatic heating with a fixed vertical profile $\Psi_2(z)$, coefficient α is determined by $\Psi_2(z)$ and precipitation scaling. The background precipitation rate $P_{r,0}$ is removed here.
	E_v	sym: $C_L C_D\left(U_b + \sqrt{(U+U_d)^2 + (V+V_d)^2}\right)(q_{sat} - q_f)$ asym: $C_L C_D\left(\sqrt{(U_b+U+U_d)^2 + (V+V_d)^2}\right)(q_{sat} - q_f)$	surface evaporation rate (dimensionless), $C_L = \begin{cases} 1.0 & \text{if } q_s > 0.75 q_{s,max} \\ \dfrac{q_s}{0.75 q_{s,max}} & \text{otherwise} \end{cases}$ is soil moisture conductivity, $C_D = 4.0$ is drag coefficient, $U_b = 0.05$ (5 m/s) is background westerly speed, U, V and U_d, V_d are the solenoidal (inferred from η) and irrotational (inferred from w) parts of total horizontal winds, q_{sat} is the saturation air moisture, and $q_{s,max}$ is the maximum soil moisture capacity.
Numerics		$3200km \times 1600km \times 16km$	domain size in x-,y-,z-directions
		$25km \times 25km \times 0.25km$	x-, y-, and z-grid spacing
		$12\ hr$	integration period
		$5\ min$	time step

then takes vertical integration with rigid boundary conditions at both the top of the atmosphere and the surface (see Appendix b). Here we further assume that the air moisture content has a fixed vertical profile (only shape, not magnitude) so that the nonlinear horizontal flux terms can be rewritten into a form without dependence on height. Such an assumption is validated (not shown) through examining the mean vertical profiles of specific humidity averaged over the central US. In brief, the column water vapor is affected by the advection effects of vertically averaged horizontal winds, precipitation, and evaporation. The third equation (the fifth row in Table 1) is for the soil moisture budget based on the bucket model (Pietschnig et al. 2021). For the sake of simplicity, both lateral flows and runoff are neglected so that the local soil moisture tendency is directly balanced by the difference between precipitation and evaporation.

Fig. 1b shows the interactions among the three model components as governed by these equations. In briefly, the PV perturbation is driven by diabatic heating, S_θ, that is dependent on air moisture, q_f, while the latter is also affected by the former through the horizontal advection effect. Precipitation, P_r, and evaporation, E_v, stand for the moisture exchange between the air and soil, the former of which is only dependent on air moisture, q_f, and the latter depends on all three components (see Table 2). In detail, the parameterization of precipitation rate, P_r, with dependence on air moisture, q_f, is obtained by fitting ERA5 reanalysis and WRF simulation data into an exponential function. The evaporation over the land is parameterized as $E_L = C_L E_{OC}$ where C_L represents the conductivity of the land surface to moisture and E_{OC} is the bulk formula for ocean surface evaporation (Pietschnig et al. 2021). Here we consider two types of evaporation schemes, that is, the symmetric and asymmetric ones. The symmetric evaporation scheme accounts for a mean evaporation rate even in the absence of winds in the free atmosphere, while the asymmetric one assumes the evaporation rate is proportional to the magnitude of total winds. The diabatic heating, $S_\theta = \frac{1}{\alpha}(P_r - P_{r,0})\Psi_2(z)$, is assumed to be proportional to precipitation anomalies, $P_r - P_{r,0}$, but has a fixed vertical profile $\Psi_2(z)$ from a WRF simulation.

b. Numerical details and simulation setup

To facilitate numerically solving the model, we first consider typical scalings for all resolved variables in Table A1 and then nondimensionalize all governing equations as shown in Eqs. A23-A27. The PV equation (Eq. A23) is solved by using the Corner-Transport Upwind (CTU) method for advection (LeVeque et al. 2002), while the PV inversion is achieved by invoking the pair of diagnostic equations (Eqs. A24-A25) and using a multigrid relaxation technique (Raymond and Jiang 1990). Both the air moisture equation (Eq. A26) and soil moisture equation (Eq. A27) are solved by using the method of lines. All variables have the periodic boundary condition in the x-direction, the Dirichlet boundary condition (constant value) in the y-direction, and the Neumann boundary condition (zero gradient) in the z-direction. Here we consider a channel domain in a size of $3200km \times 1600km \times 16km$ in the x-, y-, and z-directions. The horizontal spatial resolution is 25 km, and the vertical resolution is 0.25 km. The total integration duration of each simulation is 12 hrs, which is comparable to the typical lifetime of MCSs. The time step, $\delta t = 5min$, is chosen to be short enough to guarantee the numerical stability. To highlight the impact of each controlling

TABLE 3. Summary of all experiments conducted in this study. As shown by the 2nd-6th columns, different configurations are set through the heating (in a Fixed or Interactive magnitude), external mechanic forcing (Yes/No), initial air moisture anomaly (Yes/No), evaporation rate (Symmetric/Asymmetric), and vertical zonal wind shear (Yes/No). The last column indicates the figures resulting from corresponding experiments.

#	Heating	Mechanic forcing	Initial air moisture anomaly	Evaporation	Shear	Figure
EXP1	Interactive	Yes	No	Symmetric	No	Fig. 2
EXP2	Interactive	No	Yes	Symmetric	No	Fig. 3
EXP3	Interactive	No	Yes	Asymmetric	No	Fig. 4
EXP4	Interactive	No	Yes	Symmetric	Yes	Fig. 5
EXP5	Interactive	No	Yes	Asymmetric	Yes	Fig. 6
EXP6	Fixed	No	No	Symmetric	No	Fig. 7

factor and the corresponding physical mechanism, we run 6 sets of simulations under the same configuration with only differences in the options as shown in Table 3.

c. Input data for environmental wind and moisture fields as well as fixed vertical profiles

The model itself is an anomaly model that simulates both mesoscale circulation perturbation and moisture anomalies associated with the MCSs, which also requires several environmental profiles as input data. To obtain the mean summertime environmental profiles that are favorable for MCS initiation, we first select the hours with MCS initiation over the central U.S. ($100°W$–$90°W$) during the 14-year (2004-2007) summertime (June, July, August). This selection is achieved by using the Flexible Object Tracker algorithm (FLEXTRKR, Feng et al. 2018, 2019) and the resulting high-resolution MCS tracking database (Feng et al. 2021). Then the mean 3-D profiles of environmental temperature, $\tilde{T}(z)$, potential temperature, $\tilde{\theta}(z)$, and density, $\tilde{\rho}(z)$, and the mean 2-D horizontal profile of total column water vapor, $q_{f,0}$, are calculated based on the 14-year summertime hourly ECMWF Reanalysis v5 (ERA5) dataset. The mean 2-D horizontal profile of soil moisture (0–200 cm) is obtained by using the Phase 2 of the North American Land Data Assimilation System (NLDAS-2).

Besides, the model also assumes the fixed vertical profiles of air moisture content, $\Psi_1(z)$, and diabatic heating, $\Psi_2(z)$. $\Psi_1(z)$ is obtained by first taking the average of all domain-mean air moisture content during the MCS initiation hours over the Central U.S and then being normalized

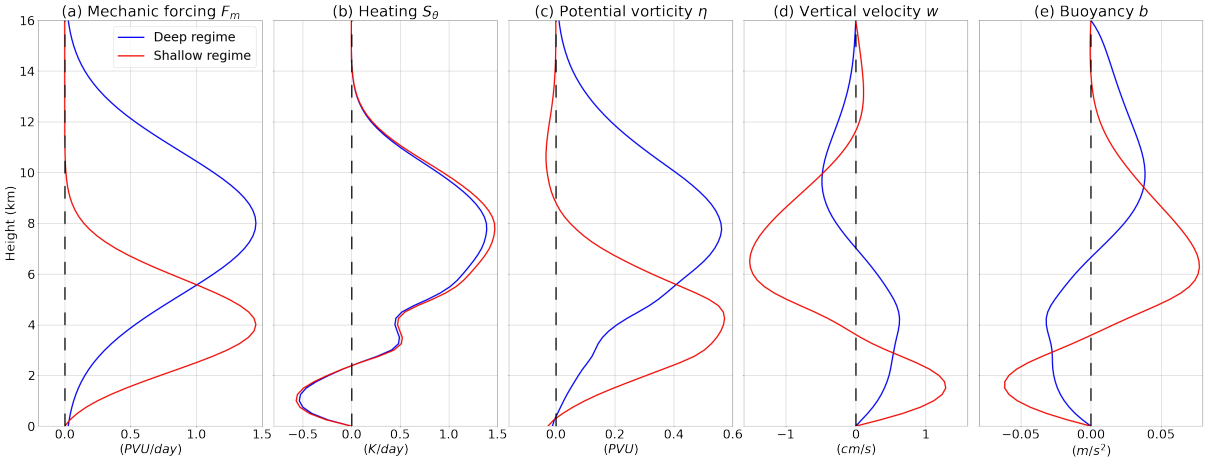

FIG. 2. Vertical profiles of mesoscale circulation fields at t = 12 hr in two different scenarios (deep, blue; shallow, red) from EXP1. Panels from left to right are for (a) mechanic forcing F_m, (b) diabatic heating S_θ, (b) PV perturbation η, (c) vertical velocity w, and (d) buoyancy anomaly b. Their dimensional units are indicated in the x-axis.

to satisfy the constraint, $[\Psi_1(z)] = 1$ (its vertical integral is equal to 1). $\Psi_2(z)$ is obtained by using a 3-month (June, July, August in 2011) WRF simulation output (Feng et al. 2018) and taking the area-weighted average of all MCSs throughout their normalized life cycle over the central U.S.

3. Mechanic and thermal forcing in initiating and intensifying MCSs

The goal of this section is to study the effects of mechanic and thermal forcing in initiating and intensifying MCSs. Two experiments (EXP1, EXP2) are considered here to highlight their effects separately. In the mechanic forcing experiment, an external mechanic forcing F_m resulting from momentum forcing is added on the right hand side of the PV (η) equation. In the thermal forcing experiment, an anomaly is added into the initial air moisture (q_f) field. Without these external F_m and air moisture anomaly, both experiments should stay in the state of rest (no winds) with balanced moisture exchange between the air and soil.

In EXP1, we further consider two different regimes (deep/shallow) with the prescribed mechanic forcing F_m reaching its maximum at different levels (see Fig. 2a), while their maximum magnitudes are set to be the same for fair comparison. The panels (b-e) in Fig. 2 show the vertical profiles of several mesoscale circulation fields at t = 12 hr as driven by the mechanic forcing. Similar to the

mechanic forcing, the resulting PV perturbation in the deep regime also reaches its maximum at height 8 km in panel (c), while that in the shallow regime is at height 4 km. In contrast, the shapes of PV perturbations are not exactly the same as the mechanic forcing, mainly due to the advection effect and the consequent diabatic heating. The resulting diabatic heating S_θ in both scenarios share the same vertical profile in panel (b), but that in the shallow regime has slightly stronger magnitude. The major differences between these two scenarios appear in the vertical velocity (panel d) and buoyancy (panel e) fields. Specifically, the vertical velocity field exhibits a dipole pattern with upper-level downdraft and lower-level updraft, while the buoyancy field also exhibits a dipole pattern with upper-level warm anomaly and lower-level cold anomaly. In comparison with the deep regime, the shallow regime features a much stronger updraft (downdraft) and cold (warm) anomaly at lower (upper) levels. The strong low-level updraft provides mechanic lifting and the low-level cold anomaly reduces convective inhibition (CIN), both of which provides favorable conditions for initiating MCSs.

Fig. 3 shows the model output from EXP2 with an initial moisture anomaly in the absence of mechanic forcing. Such a scenario can be used to mimic either the low-level moisture convergence resulting from the MCS initiation as driven by mechanic forcing in EXP1, or some pre-existing moisture anomalies due to local moisture source or remote moisture transport. Panel (a) shows the time series of moisture anomalies in both the air and soil throughout the 12-hr duration. The total domain moisture anomaly (red curve) stays in a constant value, reflecting the conservation of total moisture in the whole system. Due to the initial moisture anomaly, the air moisture starts with a positive value and keeps increasing in a linear way, while the soil moisture decays gradually. Such an increase in air moisture reflects the imbalance between evaporation and precipitation, indicating a convective instability situation where the wet regions get wetter in the free troposphere. Panel (b) shows the zonal distributions of air and soil moisture at multiple time steps. Over the convective region (1.4–1.8×10^3 km), air moisture decreases and soil moisture increases, resulting from the moisture exchange from the air to the soil with the larger precipitation than evaporation. The slightly increase of total moisture over this region should be due to the low-level moisture convergence. In contrast, air moisture increases outside of this convective region, while soil moisture decreases there. This is consistent with the positive imbalance between precipitation and evaporation over the convective region, and the negative one outside the region as shown in panel (c). Panel (d)

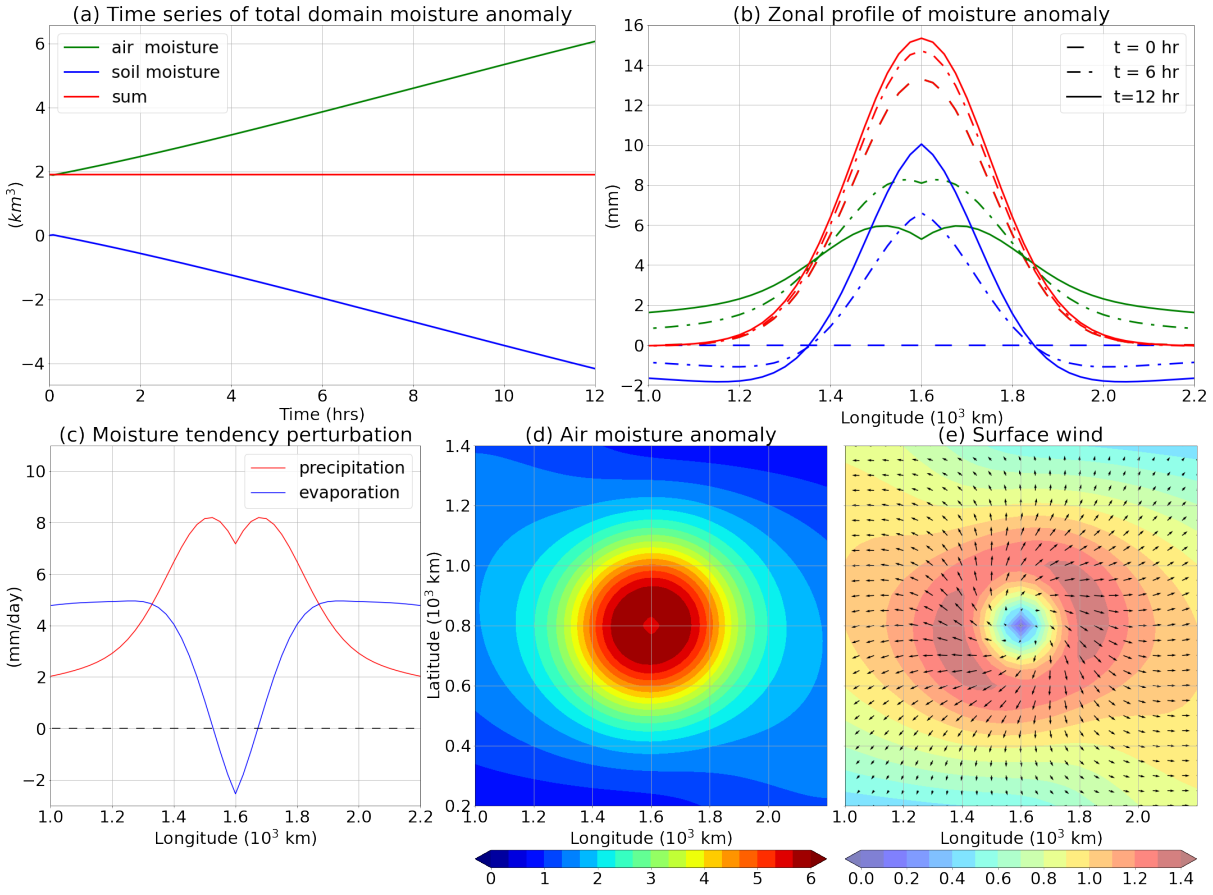

FIG. 3. Air/soil moisture anomalies, moisture tendency perturbation, and surface wind fields from EXP2. Panel (a) shows the time series of total domain moisture anomalies (air, green; soil, blue; sum, red), while panel (b) shows their zonal profiles at $t = 0, 6, 12$ hr along the central latitude $y = 800$ km. Note that the dashed green curve at $t = 0$ hr is overlapped with the dashed red curve. The prescribed environmental moisture are subtracted from the total to obtain these moisture anomalies. Panel (c) shows the zonal profiles of precipitation (red) and evaporation (blue) perturbations (relative to the background rate at the state of rest) at $t = 12$ hr along the central latitude $y = 800$ km. Panels (d) and (e) show the horizontal profiles of air moisture anomaly (color shading, mm) and and surface wind (arrows) at $t = 12$ hr. The color shading in panel (e) indicates the wind speed (m/s).

shows the horizontal distribution of air moisture, which reaches its maximum near the center and decays gradually as the distance goes further away. Panel (e) shows the horizontal profile of surface winds and their magnitude. Although the air moisture is confined over the convective region, the surface winds expand further away, promoting surface evaporation there in a longer distance. In brief, the growing air moisture is due to the surface wind driven excessive evaporation outside of

the convective region, and low-level moisture convergence for transporting moisture back to the convective region, providing a favorable condition for intensifying MCSs.

4. Effects of background surface wind and vertical wind shear on MCS propagation

The eastward propagation of MCSs at mid-latitudes is typically attributed to the zonal advection effects by background westerly jets, although their propagation speed is not necessary the same as the westerly wind speed. Here we explore several additional physical mechanisms that possibly affect the eastward propagation of MCSs, including the background surface wind and vertical wind shear. All simulations used here are initiated with an air moisture anomaly, and analyzed at $t = 12$ hours to mimic the mature stage of MCSs.

Unlike the symmetric evaporation scheme in EXP2 that retains a background evaporation rate even in the state of rest, the asymmetric evaporation scheme in EXP3 assumes that the magnitude of evaporation is proportional to the total surface wind speed (evaporation will vanish in the state of rest). Thus, the presence of a background westerly surface wind not only guarantee a background evaporation rate but also introduce the east-west asymmetry. Fig. 4 shows a direct comparison between the symmetric and asymmetric evaporation cases. In contrast to panel (a), both precipitation and evaporation rates show a clear east-west asymmetry with the precipitation peak displaced eastward and evaporation low displaced westward. Unlike the domain-wide air moisture increase in panel (b), panel (e) features only an air moisture increase to the east and a decrease to the west. As the precipitation is assumed to be proportional to air moisture (see Table 2), the changes in air moisture explains those in precipitation rate as shown in panel (d). Moreover, different from the symmetric surface wind divergence in panel (c), panel (f) for surface winds is characterized by dominant easterlies with its maximum wind speed reached to the southwest, and negligible winds in the remaining regions. In terms of total wind speed, such a westerly wind perturbation tends to cancel out with the background westerly winds, leading to the significant reduction of evaporation rate, the drying effect, to the west of the convective region. Overall, the moistening effect due to the eastward displaced air moisture anomaly and the drying effect due to the evaporation reduction to the west provides a possible mechanisms for promoting the eastward propagation of MCSs.

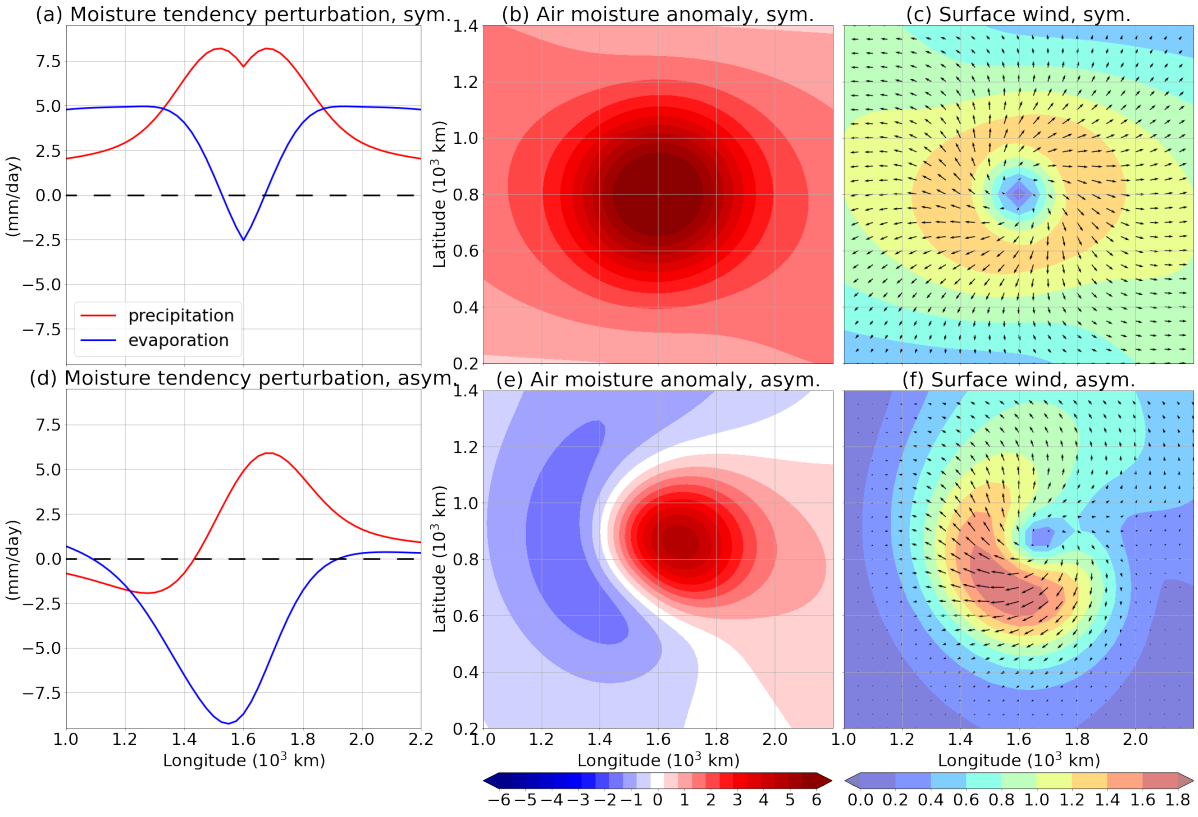

FIG. 4. Horizontal profiles of precipitation/evaporation perturbation, air moisture anomaly, and surface wind at $t = 12$ hr in two different scenarios (symmetric evaporation, top row, EXP2; asymmetric evaporation, bot row, EXP3). Panels (a,d) show the zonal profiles of precipitation/evaporation perturbation (relative to the background rate at the state of rest) along the central latitude $y = 800$ km. Panels (b,e) show the horizontal profiles of air moisture anomalies (color shading, mm), while panels (c,f) are for surface wind (arrows). Note that panels (a-c) are the same as Fig. 3c-e but in a different colorbar. We repeat them here for comparison. The color shading in panel (e) indicates the wind speed (m/s).

Besides the background surface winds, the background vertical wind shear is another factor for promoting the eastward propagation of MCSs. Fig 5a shows the vertical profiles of domain-averaged background zonal winds over the central U.S, which are typically dominated by westerly winds with its maximum reached at height 12 km. Panels (c-e) show the longitude-height cross-section of vertical velocity in different cases (no shear, weak shear, strong shear). All three scenarios feature a vertical dipole pattern with an upper-level updraft and a lower-level downdraft over the convective region. As the shear strength increases, the vertical structure of vertical velocity tilts

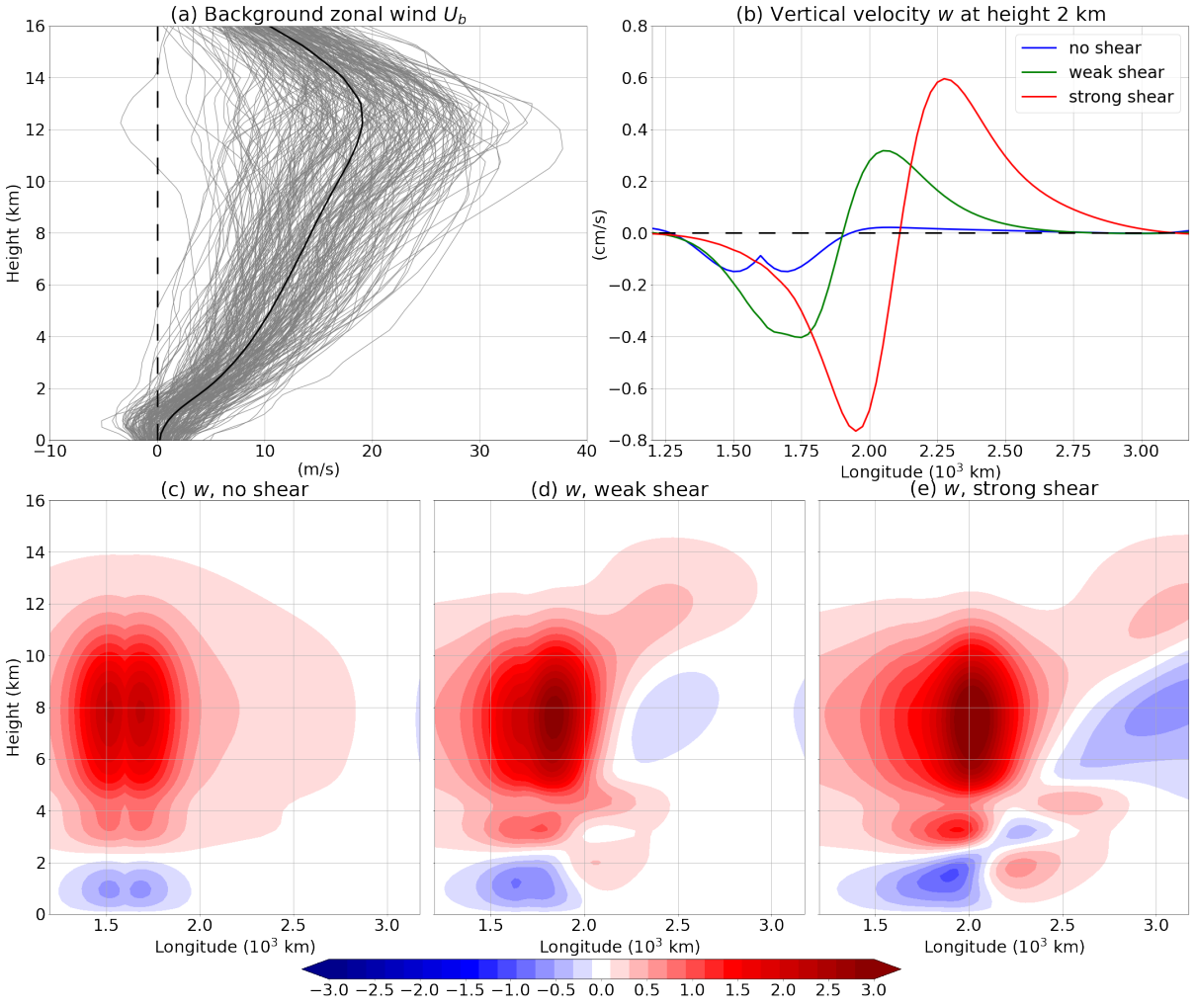

FIG. 5. Vertical velocity field at $t = 12$ hr in three different scenarios from EXP4. Panel (a) shows background zonal wind U_b averaged over the central US during 2004-2017 summer-time (JJA) MCS initiation events (250 events in total). Black curve stands for the mean profile. Panel (b) shows the zonal profile of vertical velocity at height 2 km along the central latitude $y = 800$ km. Panels (c-e) show the vertical cross section of vertical velocity in the scenario with (c) no shear, (d) weak shear, (e) strong shear. The dimensional unit of w is cm/s.

eastward, simply due to the mean wind advection effect. More importantly, both the weak and strong shear cases in panels (d, e) also feature an updraft perturbation appears to the east, which is absence in the no shear case in panel (c). Panel (b) further indicates that this updraft perturbation has a stronger magnitude as the strength of background vertical wind shear increases, providing

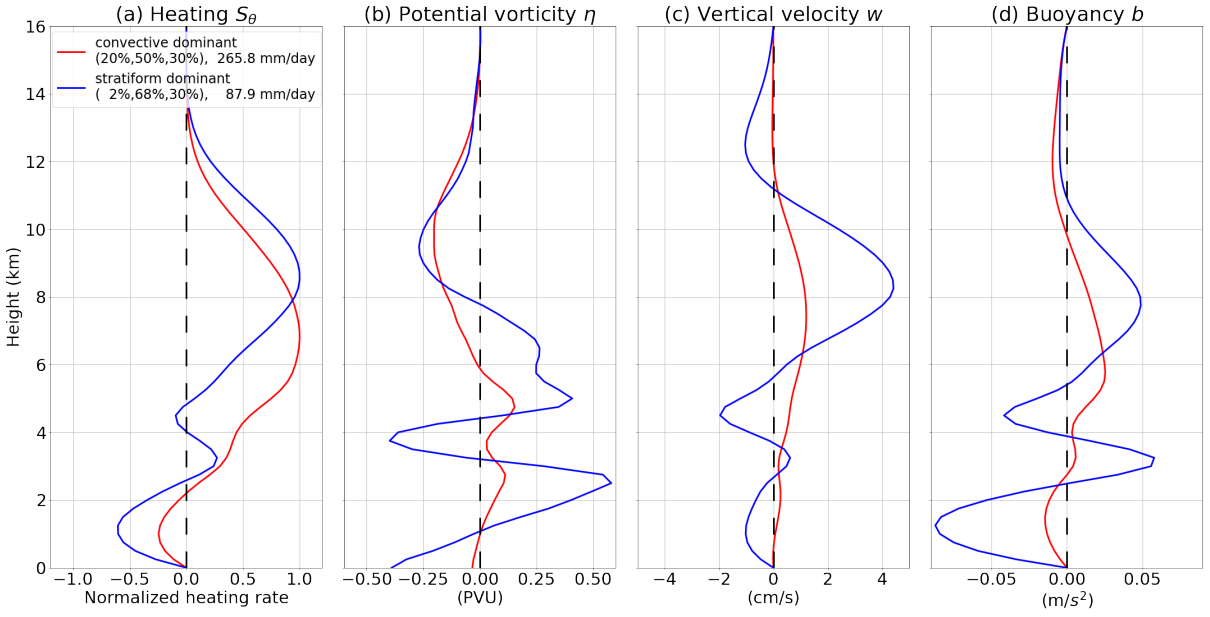

FIG. 6. Vertical profiles of mesoscale circulation fields $t = 12$ hr in two different scenarios (convective dominant, blue; stratiform dominant, red) from EXP5 Panels from left to right are for (a) diabatic heating S_θ, (b) PV perturbation η, (c) vertical velocity w, and (d) buoyancy anomaly b. The three percentage numbers inside the parenthesis indicates the fractions of convective, stratiform, and other type clouds. Their dimensional units are indicated in the x-axis.

a favorable condition for triggering new convection to the east. The vertical wind shear induced low-level updraft provides another mechanism for promoting the eastward propagation of MCSs.

5. The role of stratiform heating on MCS dynamics

Recall that in this study, the fixed vertical profile of diabatic heating, $\Psi_2(z)$ is obtained by taking the average of all MCSs throughout their life cycles. In reality, the actual diabatic heating profile should vary at different life stages with changing fractions of convective and stratiform cloud types. It is worthwhile to investigate how different diabatic heating profiles would eventually influence the mesoscale circulation response as well as precipitation intensity, particularly about the stratiform heating.

Fig. 6a shows the vertical profiles of diabatic heating resulting from different fractions of convective and stratiform type clouds. The stratiform dominant heating with a larger stratiform cloud fraction reaches its maximum at height 9 km, 2 km higher than the convective dominant

heating. Moreover, the stratiform dominant heating features a stronger low-level cooling below the height 2 km as well as a dipole pattern at height 4 km, which should be attributed to the complex stratiform cloud heating pattern as diagnosed from the WRF simulation. It is also worth mentioning that compared with the convective dominant heating, the stratiform dominant heating in the same maximum magnitude corresponds a much lower surface precipitation intensity, largely due to the rain evaporation in the downdraft regions. For PV perturbation in panel (b), the stratiform dominant heating case features an alternate pattern of PV perturbations below height 8 km, in contrast to the positive PV perturbations in the convective dominant heating case. For vertical velocity in panel (c), the stratiform dominant heating case is characterized by a stronger upper-level updraft and lower-level downdraft, while that in the convective dominant heating case is much weaker. Similarly, such an enhanced mesoscale circulation is also seen in the buoyancy field in panel (d). Overall, the mesoscale circulation fields driven by the stratiform dominant heating have a much stronger magnitude than those driven by the convective dominant heating. It is shown here that the stratiform dominant heating is more efficient (with less precipitation intensity) to drive mesoscale circulation response, and thus play a crucial role in controlling the mesoscale circulation associated with MCSs.

That said, it is difficult to seek a thorough and clear investigation about the role of stratiform heating in EXP5 with the initial air moisture anomaly, asymmetric evaporation rate with background surface winds, and background vertical wind shear (see Table 3). Fig. 7 shows the vertical profiles of various mesoscale circulation fields in a much simpler setup, which are solely driven by three prescribed steady heating (shallow, deep, stratiform). As shown by panel (a), these three heating types mimic the typical diabatic heating profiles associated with shallow congestus, deep convective, and stratiform cloud convection with major differences in the maximum heating height. The stratiform heating also features a weak cooling at lower levels, mainly due to rain evaporation. For PV perturbation in panel (b), both shallow and deep heating induce a dipole pattern with upper-level negative PV perturbations and lower-level positive ones. In contrast, the stratiform heating case also features another negative PV perturbation below the mid-level positive PV perturbation. Unlike the shallow and deep heating cases with updraft throughout the troposphere in panel (c), the stratiform heating cases is characterized by a much upper-level updraft and a lower-level downdraft. Similar to the vertical velocity pattern, the buoyancy field in

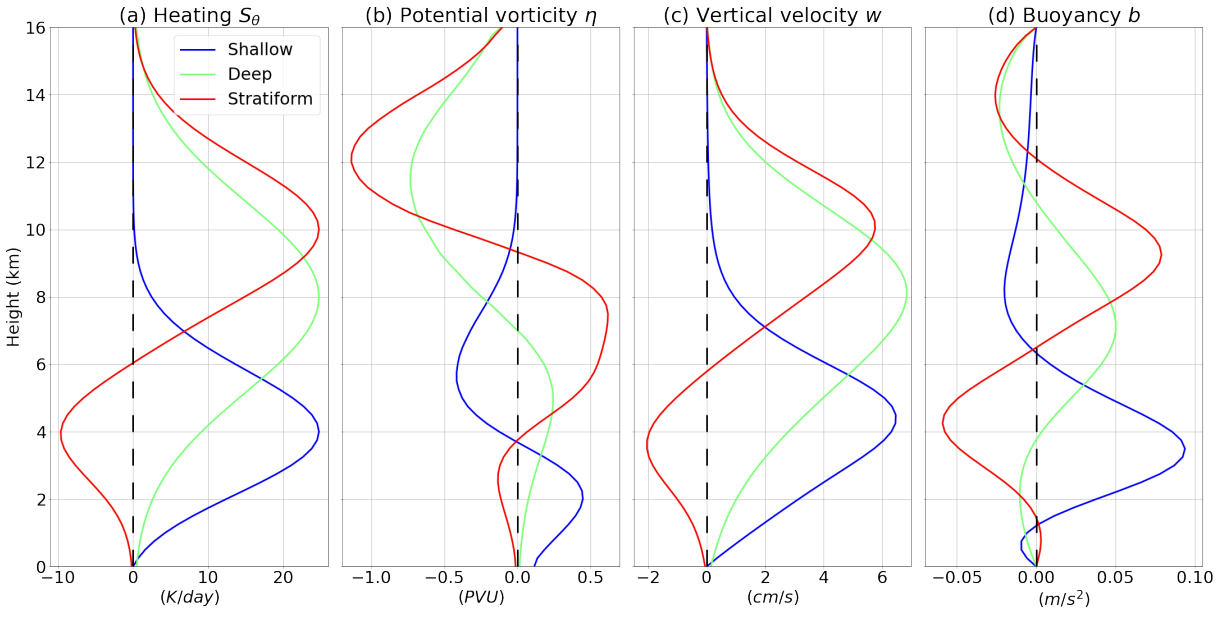

394 FIG. 7. Vertical profiles of mesoscale circulation fields t = 12 hr in three different scenarios (shallow, blue;
395 deep, green; stratiform, red) from EXP6. Panels from left to right are for (a) diabatic heating S_θ, (b) PV
396 perturbation η, (c) vertical velocity w, and (d) buoyancy anomaly b. Their dimensional units are indicated in the
397 x-axis.

412 the stratiform heating case also features a cold anomaly at lower levels. In brief, when compared
413 with the shallow and deep heating cases, the stratiform heating case is manifested by elevated PV
414 perturbations, updraft, and positive buoyancy fields as well as additional weak anomalies at lower
415 levels in the opposite sign, resembling the observed mid-latitude continental MCS (see Figure 19
416 of Knievel and Johnson (2002)).

417 ## 6. Concluding discussion

429 Fig. 8 summarizes the major findings in this study about the underlying physical mechanisms
430 for the initiation, intensification, and eastward propagation of mid-latitude MCSs over the land. At
431 the MCS initiation stage, the external mechanic forcing (cyclonic red arrows) induces the positive
432 PV perturbations (red cloud symbol) along with the lower-level updrafts (black arrows), the latter
433 of which provides a favorable condition for triggering new convection. At the MCS intensification
434 stage, the surface wind (black arrows) driven evaporation (upward red arrows) is enhanced over
435 the region far away from the convection center. Then these extra moisture from the enhanced

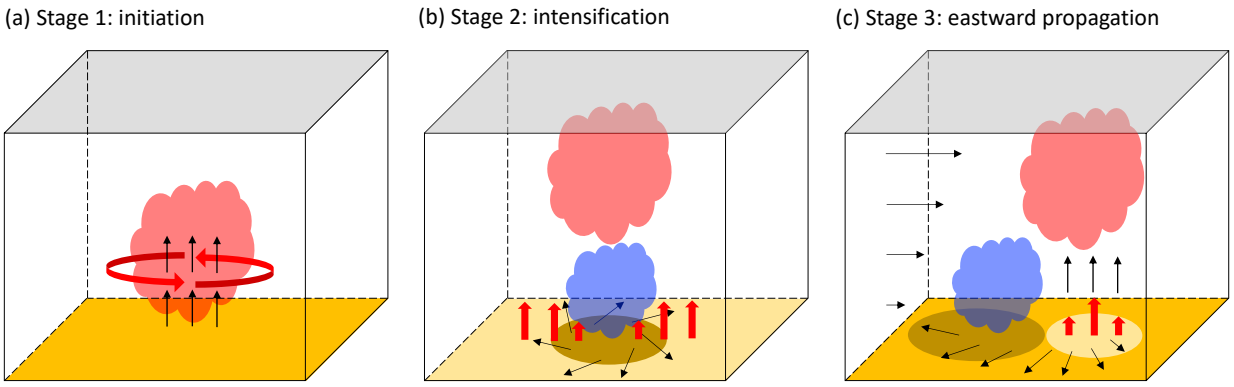

FIG. 8. Schematic diagram for physical mechanisms responsible for the initiation, intensification, and eastward propagation of the MCSs simulated in this simple model. Panel (a) shows the initiation stage where mechanical forcing (circular arrows) induces updraft (black arrows) and positive PV perturbation (red cloud) at lower troposphere in the presence of moderate soil moisture (yellow). Panel (b) shows the intensification stage where initial moisture anomalies resulting from updraft in (a) induce strong surface winds (black arrows) and enhance surface evaporation rate (red arrows), leading to upper-tropospheric positive PV perturbations (red cloud) and lower-tropospheric negative PV perturbations (blue cloud). Soil moisture increases near the convective regions (dark yellow) but decreases beyond that region (light yellow). Panel (c) shows the eastward propagation stage where vertical shear of zonal winds (eastward black arrows at the left) induces updraft to the east, and asymmetric evaporation rate leads to stronger evaporation to the east than west in the presence of background surface westerlies.

evaporation is transported back to the convective area due to the low-level moisture convergence, leading to a positive feedback to further intensify the MCS convection. As for the eastward propagation of MCSs, the presence of background surface westerlies induces stronger evaporation to the east, and the presence of background westerly vertical wind shear further induces low-level updraft to the east, both of which provides favorable conditions for triggering new convection to the east and promoting the MCS eastward propagation. Besides, the result also highlights the crucial role of stratiform heating in inducing larger mesoscale circulation response and affecting their vertical structures.

The source of mechanic forcing we discussed in this study can be attributed to the eastward-moving subsynoptic disturbances from the Rocky Mountains or even further western regions over the northern Pacific. For example, Li and Smith (2010) conducted harmonic analysis of

observational date from 10000 Automated Surface Observing System (ASOS) stations and detected eastward-moving PV anomalies east of the Rockies. Wang et al. (2011a) used the North American Regional Reanalysis (NARR) to trace mid-tropospheric perturbations (MPs), and found that the persistent ascending motion at the leading edge of MPs promotes convection and its downstream propagation assists in forming the progressive feature of convective storms. Pokharel et al. (2019) also concluded the triggering mechanism of the eastward propagating MPs for progressive MCSs. Tuttle and Davis (2013) used a 10-year NCEP NARR data to objectively identify and track short waves in the north American domain and concluded with their modulation effects on the diurnal cycle of warm-season precipitation. Song et al. (2021) conducted a self-organizing map analysis to identify the summertime MCS initiation environments and concluded that MCSs associated with MPs produce more rainfall in a larger area and a stronger convective intensity. The result here demonstrates a fundamental mechanism for mechanic forcing from those eastward-propagating disturbances in initiating MCSs.

This study identifies a positive feedback mechanism among surface wind, evaporation, and moisture, which serves as a mid-latitude land analogue to the wind-induced surface heat exchange (WISHE, Yano and Emanuel 1991) mechanism that was originally found over the tropical ocean. Also, the total moisture (air + soil) keeps increasing over the convective region, reproducing the typical scenario that wet regions get wetter and dry regions get drier as seen in the convective self-aggregation phenomenon (Held et al. 1993; Bretherton et al. 2005; Wing et al. 2017). The simple bucket model for soil moisture dynamics and the evaporation scheme used in this study highlights the possible impact of soil moisture on MCS initiation and propagation. Hu et al. (2021b) used a unique combination of rainfall events in observations and land surface simulations with numerical tracers to quantify soil moisture source and found that soil moisture sourced from early warm-season MCS rainfall is important for initiating summer afternoon rainfall. This model provides a simple framework to describe the convective instability, upscale growth, soil moisture feedback mechanisms relevant to the mid-latitude MCSs over the land.

This study also demonstrates the crucial role of background surface westerlies and vertical westerly wind shear in triggering new convection to the east and promoting the eastward propagation of MCSs. In fact, it is still a difficult task to predict warm-season MCS movement over the Great Plains by using many methods, including the statistical procedure (Corfidi et al. 1996), numerical

models (Stensrud et al. 2000; Pinto et al. 2015), and machine learning techniques (Ahijevych et al. 2016; Zhang et al. 2019). The result suggests the useful role of background surface winds and vertical wind shear as additional precursors for predicting MCS movement.

The key role of stratiform heating on determining precipitation intensity and shaping mesoscale circulation response is investigated here by varying the prescribed diabatic heating profile. Due to the assumption of scale separation, traditional cumulus parameterization in the GCMs poorly represents the stratiform heating (Molinari 1993), although several encouraging progresses have been made in the recent years. By adding stratiform-like heating structure and cooling into the NCAR Community Atmosphere Model version 5.3 (CAM5.3), Cao and Zhang (2017) reproduced many observed features of the MJO that are missing otherwise. Such an improvement is also seen for the MJO and monsoon intraseasonal oscillation simulations in a coarse resolution aquaplanet GCM (Deng et al. 2016; Ajayamohan et al. 2016). Moncrieff et al. (2017) first developed a new approach for treating organized convection in GCMs, the MCSP, to introduce the missing stratiform heating and convective momentum transport (CMT) associated with MCSs. This MCSP scheme was implemented in CAM5.5 (Moncrieff 2019) and the Energy Exascale Earth System Model version 1 (E3SMv1) (Chen et al. 2021a), and proved to be useful for improving large-scale precipitation patterns and tropical wave modes.

This moist PV model in the current form can be elaborated and extended in several ways. Several important factors and processes are currently ignored for the sake of simplicity, but could potentially play an important role in affecting MCSs, such as the radiation, surface fluxes, and divergent flows (due to scaling assumption). Besides, the initiation and upscale growth of mid-latitude MCSs can be not only from either convective instability but also the baroclinic instability of large-scale flows. It is interesting to further extend this model into a larger-scale framework that is capable to simulate MCSs and baroclinic instability simultaneously, which should be then useful to study the interactions between MCSs and large-scale environments. Lastly, this simple PV model can also serve as a diagnostic framework for studying the possible relation between pre-existing PV anomalies and MCS initiation.

Acknowledgments. This research is supported by the U.S. Department of Energy Office of Science Biological and Environmental Research as part of the Regional and Global Model Analysis program area. PNNL is operated for the Department of Energy by Battelle Memorial Institute under contract DE-AC05-76RL01830.

Data availability statement. The ERA5 hourly data for mean environmental profiles can be downloaded from the Climate Data Store (CDS) website (`https://cds.climate.copernicus.eu/cdsapp#!/dataset/reanalysis-era5-pressure-levels?tab=form`). The NLDAS-2 data for soil moisture can be downloaded from the NASA Goddard Earth Sciences (GES) Data and Information Services Center (DISC) (`https://disc.gsfc.nasa.gov/datasets/NLDAS_NOAH0125_H_2.0/summary?keywords=NLDAS`). The WRF simulation output for 2011 summertime MCSs over the U.S. can be downloaded by referring to the acknowledgments part of Feng et al. (2018). All model output and plotting scripts in this study are available on application to the corresponding author.

APPENDIX

Derivation of the moist model for mid-latitude MCSs over the land

The derivation of the model follows Raymond and Jiang (1990) with only a few minor modifications. The major improvement here is to extend Raymond and Jiang (1990)'s dry model into a moist version by coupling air and soil moisture through moisture exchange processes.

To derive the governing equations, we start from the f-plane primitive equations in the anelastic approximation (Bannon 1996) along with air and soil moisture budget equations,

$$\frac{Du}{Dt} - fv = -\phi_x - \frac{1}{\tau}u + F_u, \tag{A1}$$

$$\frac{Dv}{Dt} + fu = -\phi_y - \frac{1}{\tau}v + F_v, \tag{A2}$$

$$\frac{Db}{Dt} + N^2 w = \frac{g}{\tilde{\theta}} S_\theta, \tag{A3}$$

$$\phi_z = b, \tag{A4}$$

$$u_x + v_y + \frac{1}{\tilde{\rho}}\left(\tilde{\rho} w\right)_z = 0, \tag{A5}$$

$$\frac{Dq_f}{Dt} = -\frac{1}{\tilde{\rho}} P_r - \frac{1}{\tilde{\rho}} \frac{\partial}{\partial z} E_v, \tag{A6}$$

$$\frac{\partial q_s}{\partial t} = P_r - E_v, \tag{A7}$$

where $\frac{D}{Dt} = \frac{\partial}{\partial t} + u\frac{\partial u}{\partial x} + v\frac{\partial v}{\partial y} + w\frac{\partial w}{\partial z}$ is material derivative, u, v, w (unit: m/s) are zonal, meridional, and vertical winds, $\phi = \frac{p'}{\tilde{\rho}}$ (unit: m^2/s^2) is pressure perturbation, $b = g\frac{\theta'}{\tilde{\theta}}$ (unit: m/s^2) is buoyancy anomaly , q_f (unit: kg/kg) is specific humidity, and q_s (unit: kg/m^3) are soil moisture content, respective. The damping terms $-\frac{1}{\tau}u$, $-\frac{1}{\tau}v$ are for Rayleigh friction (Romps 2014), and (F_u, F_v) are for external mechanic forcing. $S_\theta = \frac{\tilde{\theta}}{C_p \tilde{T}}\dot{Q}$ is diabatic heating (latent heat plus radiative cooling). P_r and E_v stand for precipitation and surface evaporation rates, respectively. $N^2 = \frac{g}{\tilde{\theta}}\frac{\partial \tilde{\theta}}{\partial z}$ is Brunt-Väisälä frequency. Here $\tilde{\rho}, \tilde{\theta}, \tilde{T}$ are environmental density, potential temperature, and temperature profiles, while p', and θ' are actual pressure and potential temperature anomalies.

a. Governing equations for PV dynamics

According to the Helmholtz decomposition, the 2-D horizontal wind fields can be represented as the sum of solenoidal (represented by ψ) and irrotational (represented by ζ) parts,

$$u = -\psi_y - \zeta_x, \tag{A8}$$

$$v = \psi_x - \zeta_y, \tag{A9}$$

where ψ and ζ are stream function and velocity potential, respectively. It is assumed that both the irrotational part and vertical velocity are secondary on the mesoscale. Then the absolute vorticity can be written as, $\overrightarrow{\xi}_a = \overrightarrow{\xi} + f\overrightarrow{k} = \left(-\psi_{xz}, -\psi_{yz}, \Delta\psi + f\right)$, and the Ertel PV can be written as,

$$q = \frac{1}{\tilde{\rho}}\overrightarrow{\xi}_a \cdot \nabla\theta = \frac{1}{\tilde{\rho}}\left[-\psi_{xz}\theta_x - \psi_{yz}\theta_y + (\Delta\psi + f)\,\theta_z\right]. \tag{A10}$$

Given a reference state $\theta = \tilde{\theta} + \theta'$, we split the PV into ambient and perturbation parts, $q = \tilde{q} + q'$, where $\tilde{q} = \frac{f}{\tilde{\rho}}\frac{\partial\tilde{\theta}}{\partial z}$ and

$$\frac{g\tilde{\rho}}{\tilde{\theta}}q' = \frac{f}{\tilde{\theta}}\left(\tilde{\theta}\phi_z\right)_z + N^2\Delta\psi - \left(\psi_{xz}\phi_{xz} + \psi_{yz}\phi_{yz}\right). \tag{A11}$$

The hydrostatic balance $\phi_z = b$ in Eq. A4 and $b = g\frac{\theta'}{\tilde{\theta}}$ are used to derive the above expression. Also, the term $\Delta\psi(\theta')_z$ is ignored for simplicity.

By assuming the winds are dominated by the solenoidal part, $u = -\psi_y$ and $v = \psi_x$ (thus $u_x + v_y = 0$ and $w = 0$), we can obtain the following balance condition based on Eqs. A1-A2,

$$\Delta\left(\phi - f\psi\right) = 2\psi_{xx}\psi_{yy} - 2\left(\psi_{xy}\right)^2. \tag{A12}$$

Given the PV value q', Eqs. A11-A12 form a diagnostic pair and can be used to infer ψ and ϕ.

According to the Ertel's Theorem (Pedlosky et al. 1987), the PV obeys the following equation,

$$\frac{Dq}{Dt} = \frac{1}{\tilde{\rho}}\nabla\cdot\left(S_\theta\overrightarrow{\xi}_a + \theta\nabla\times\overrightarrow{F}\right), \tag{A13}$$

where S_θ is the diabatic heating, $\overrightarrow{F}$ is the momentum forcing. By only focusing on PV perturbation and buoyancy anomalies in Eq. A3, we can obtain,

$$q'_t - \psi_y q'_x + \psi_x q'_y + w\tilde{q}_z = \frac{1}{\tilde{\rho}}\nabla\cdot\left(S_\theta\overrightarrow{\xi}_a\right) - \frac{1}{\tau}q' + \overrightarrow{F}, \tag{A14}$$

$$b'_t - \psi_y b'_x + \psi_x b'_y + wN^2 = \frac{g}{\tilde{\theta}}S_\theta, \tag{A15}$$

where we ignore the vertical advection of PV perturbation term $w'q'_z$. We also replace $\overrightarrow{F}$ in Eq. A13 by $\left(-\frac{1}{\tau}u + F_u, -\frac{1}{\tau}v + F_v, 0\right)$ and rewrite the external mechanic forcing $\frac{1}{\tilde{\rho}}\nabla\cdot\left(\theta\nabla\times\overrightarrow{F}\right)$ as F_m.

Now we introduce a reduced PV perturbation,

$$\eta = q' - \frac{\tilde{q}_z}{N^2} b', \tag{A16}$$

which satisfying the following equation,

$$\eta_t - \psi_y \eta_x + \psi_x \eta_y = \frac{1}{\tilde{\rho}} \left[\nabla \cdot \left(S_\theta \overrightarrow{\xi}_a \right) - f \frac{\tilde{q}_z}{\tilde{q}} S_\theta \right] - \frac{1}{\tau} \eta + F_m, \tag{A17}$$

where we replace the linear damping term $-\frac{1}{\tau} q'$ by $-\frac{1}{\tau} \eta$ for simplicity. Furthermore, by using Eq. A16, we can rewrite Eq. A11 as

$$\frac{g\tilde{\rho}}{\tilde{\theta}} \eta = \frac{f\tilde{q}}{\tilde{\theta}} \left(\frac{\tilde{\theta}}{\tilde{q}} \phi_z \right)_z + N^2 \Delta \psi - \left(\psi_{xz} \phi_{xz} + \psi_{yz} \phi_{yz} \right). \tag{A18}$$

Now we complete derivation of the governing equations in Eqs. A17, A18, A12 for PV dynamics. This PV model resolves the prognostic variable η in Eq. A17, while ψ and ϕ are inferred through PV inversion in Eqs. A18 and A12. The solenoidal part (dominant magnitude) of u, v represented by streamfunction ψ is inferred from ψ and buoyancy anomaly b is inferred from Eq. A4. The vertical velocity w is obtained diagnostically by using Eq. A15. Then the irrotational part (secondary magnitude) of u, v represented by ζ is inferred from w.

b. Governing equations for air and soil moisture

By using Eqs. A5 and A6, we can rewrite the specific humidity budget equation into a flux form,

$$\left(\tilde{\rho} q_f \right)_t + \left(u \tilde{\rho} q_f \right)_x + \left(v \tilde{\rho} q_f \right)_y + \left(w \tilde{\rho} q_f \right)_z = -P_r - \frac{\partial}{\partial z} E_v. \tag{A19}$$

For an arbitrary profile f, here we introduce column integrated operator $[f]$ defined as,

$$[f] = \int_0^H f \, dz, \tag{A20}$$

where $z = 0, H$ correspond to the surface and top of the troposphere, respectively. After vertically integrating Eq. A19, we reach the column air moisture budget equations as follows,

$$\left[\tilde{\rho} q_f\right]_t + \left[u\tilde{\rho} q_f\right]_x + \left[v\tilde{\rho} q_f\right]_y = -\left[P_r\right] + E_v, \tag{A21}$$

where the vertical flux term vanishes due to rigid boundary condition ($w = 0$, at $z = 0, H$). For simplicity, we further assume air moisture content has a fixed vertical profile $\Psi_1(z)$ that satisfies $[\Psi_1(z)] = 1$. We can rewrite $\tilde{\rho} q_f = \rho_w \bar{q} \Psi_1(z)$, where ρ_w is liquid water density and $\bar{q}$ is total column water vapor. Then we can obtain the column water vapor budget equation $\bar{q}_t + \left([u\Psi_1]\,\bar{q}\right)_x + \left([v\Psi_1]\,\bar{q}\right)_y = -\frac{1}{\rho_w}\left[P_r\right] + \frac{1}{\rho_w} E_v$, and rewrite it as follows,

$$\left(q_f\right)_t + \left([u\Psi_1]\, q_f\right)_x + \left([v\Psi_1]\, q_f\right)_y = -P_r + E_v, \tag{A22}$$

where we replace $\bar{q}, \frac{1}{\rho_w}\left[P_r\right], \frac{1}{\rho_w} E_v$ by q_f, P_r, E_v without causing confusion of notation.

The derivation of local soil moisture budget equation follows the bucket model as explained in Pietschnig et al. (2021). The governing equation just reads as Eq. A7, where q_s stands for total moisture content in the column soil from the surface to a certain underground level. Both lateral flows and runoff are neglected here for simplicity.

c. Nondimensionalization of all governing equations

For the convenience to numerically solve this model, we first introduce scalings for all variables and coordinates in Table A1 to nondimensionalize all the governing equations (Eqs. A17, A18, A12, A22 and A7).

TABLE A1. Scalings for all variables and coordinates to nondimensionalize all the governing equations in the model. The notation hat indicates dimensionless variables. The value in the second column corresponds to the scaling before the dimensionless variable in the first column.

Variable	Scaling	Description
$N = \mathcal{N}\hat{N}$	0.01 $1/s$	buoyancy frequency scale
$z = H\hat{z}$	10 km	height scale
$(u, v) = \mathcal{N}H\,(\hat{u}, \hat{v})$	100 m/s	horizontal velocity scale
$t = \frac{1}{f}\hat{t}$	2.96 hr	time scale
$(x, y) = \frac{\mathcal{N}H}{f}\,(\hat{x}, \hat{y})$	1067.0 km	length scale
$w = Hf$	0.94 m/s	vertical velocity scale
$\tilde{\theta} = \Theta\hat{\tilde{\theta}}$	300.0 K	environmental temperature scale
$\tilde{\rho} = R\hat{\tilde{\rho}}$	1.2 kg/m^3	environmental density scale
$\eta = \frac{f\Theta\mathcal{N}^2}{Rg}\hat{\eta}$	0.24 PVU	PV perturbation scale
$\psi = \frac{\mathcal{N}^2H^2}{f}\hat{\psi}$	$1.07 \times 10^8 m^2/s$	streamfunction scale
$\phi = \mathcal{N}^2H^2\,\hat{\phi}$	$1.0 \times 10^4 m^2/s^2$	pressure perturbation scale
$S_\theta = \frac{\mathcal{N}^2H\Theta f}{g}\hat{S}_\theta$	247.7 K/day	diabatic heating scale
$b = \mathcal{N}^2H\hat{b}$	1.0 m/s^2	buoyancy anomaly scale
$(P_r, E_v) = P\,(\hat{P}_r, \hat{E_v})$	216.0 mm/day	precipitation/evaporation scale
$(q_f, q_s) = \frac{P}{f}\,(\hat{q}_f, \hat{q}_s)$	26.7 mm	moisture anomaly scale

After replacing the scaling for all variables and coordinates in Table 1, the governing equations in dimensionless units read as follows (the notation hat is dropped for simplicity),

$$\eta_t - \psi_y\eta_x + \psi_x\eta_y = \frac{1}{\tilde{\rho}}\left[\nabla\cdot\left(S_\theta\overrightarrow{\xi}_a\right) - \frac{\tilde{q}_z}{\tilde{q}}S_\theta\right] - \frac{1}{\tau}\eta + F_u, \tag{A23}$$

$$\frac{1}{\tilde{\theta}\tilde{q}}\eta = \frac{\tilde{q}}{\tilde{\theta}^2N^2}\left(\frac{\tilde{\theta}}{\tilde{q}}\phi_z\right)_z + \frac{1}{\tilde{\theta}}\Delta\psi - \frac{1}{N^2\tilde{\theta}}\left(\psi_{xz}\phi_{xz} + \psi_{yz}\phi_{yz}\right), \tag{A24}$$

$$\Delta\left(\phi - \psi\right) = 2\psi_{xx}\psi_{yy} - 2\left(\psi_{xy}\right)^2, \tag{A25}$$

$$\left(q_f\right)_t + \left(\left[u\Psi_1(z)\right]q_f\right)_x + \left(\left[v\Psi_1(z)\right]q_f\right)_y = -P_r + E_v, \tag{A26}$$

$$\left(q_s\right)_t = P_r - E_v. \tag{A27}$$

References

Ahijevych, D., J. O. Pinto, J. K. Williams, and M. Steiner, 2016: Probabilistic forecasts of mesoscale convective system initiation using the random forest data mining technique. *Weather and Forecasting*, **31 (2)**, 581–599.

588 Ajayamohan, R., B. Khouider, A. J. Majda, and Q. Deng, 2016: Role of stratiform heating on the
589 organization of convection over the monsoon trough. *Climate Dyn.*, **47 (12)**, 3641–3660.

590 Anderson, C. J., and R. W. Arritt, 1998: Mesoscale convective complexes and persistent elongated
591 convective systems over the united states during 1992 and 1993. *Mon. Wea. Rev.*, **126 (3)**,
592 578–599.

593 Bannon, P. R., 1996: On the anelastic approximation for a compressible atmosphere. *J. Atmos.*
594 *Sci.*, **53 (23)**, 3618–3628.

595 Betts, A., R. Grover, and M. Moncrieff, 1976: Structure and motion of tropical squall-lines over
596 venezuela. *Quart. J. Roy. Meteor. Soc.*, **102 (432)**, 395–404.

597 Brenowitz, N., A. Majda, and Q. Yang, 2018: The multiscale impacts of organized convection in
598 global 2-d cloud-resolving models. *JAMES*, **10 (8)**, 2009–2025.

599 Bretherton, C. S., P. N. Blossey, and M. Khairoutdinov, 2005: An energy-balance analysis of deep
600 convective self-aggregation above uniform sst. *J. Atmos. Sci.*, **62 (12)**, 4273–4292.

601 Cao, G., and G. J. Zhang, 2017: Role of vertical structure of convective heating in MJO simulation
602 in ncar cam5. 3. *J. Climate*, **30 (18)**, 7423–7439.

603 Chen, C.-C., J. Richter, C. Liu, M. Moncrieff, Q. Tang, W. Lin, S. Xie, and P. J. Rasch, 2021a:
604 Effects of organized convection parameterization on the mjo and precipitation in E3SMv1. part
605 i: Mesoscale heating. *JAMES*, **13 (6)**, e2020MS002 401.

606 Chen, X., L. R. Leung, Z. Feng, and F. Song, 2022a: Crucial role of mesoscale convective systems
607 in the vertical mass, water, and energy transports of the south asian summer monsoon. *J. Climate*,
608 **35 (1)**, 91–108.

609 Chen, X., L. R. Leung, Z. Feng, F. Song, and Q. Yang, 2021b: Mesoscale convective systems
610 dominate the energetics of the south asian summer monsoon onset. *Geophys. Res. Lett.*, **48 (17)**,
611 e2021GL094 873.

612 Chen, X., L. R. Leung, Z. Feng, and Q. Yang, 2022b: Precipitation-moisture coupling over tropical
613 oceans: Sequential roles of shallow, deep, and mesoscale convective systems. *Geophys. Res.*
614 *Lett.*, **49 (7)**, e2022GL097 836.

615 Coniglio, M. C., J. Y. Hwang, and D. J. Stensrud, 2010: Environmental factors in the upscale
616 growth and longevity of mcss derived from rapid update cycle analyses. *Mon. Wea. Rev.*, **138 (9)**,
617 3514–3539.

618 Coniglio, M. C., D. J. Stensrud, and M. B. Richman, 2004: An observational study of derecho-
619 producing convective systems. *Weather and forecasting*, **19 (2)**, 320–337.

620 Corfidi, S., J. Meritt, and J. Fritsch, 1996: Predicting the movement of mesoscale convective
621 complexes. *Weather and Forecasting*, **11 (1)**, 41–46.

622 Deng, Q., B. Khouider, A. J. Majda, and R. Ajayamohan, 2016: Effect of stratiform heating on the
623 planetary-scale organization of tropical convection. *J. Atmos. Sci.*, **73 (1)**, 371–392.

624 Feng, Z., R. A. Houze, L. R. Leung, F. Song, J. C. Hardin, J. Wang, W. I. Gustafson, and
625 C. R. Homeyer, 2019: Spatiotemporal characteristics and large-scale environments of mesoscale
626 convective systems east of the rocky mountains. *J. Climate*, **32 (21)**, 7303–7328.

627 Feng, Z., L. R. Leung, S. Hagos, R. A. Houze, C. D. Burleyson, and K. Balaguru, 2016: More
628 frequent intense and long-lived storms dominate the springtime trend in central us rainfall.
629 *Nature communications*, **7 (1)**, 1–8.

630 Feng, Z., L. R. Leung, R. A. Houze Jr, S. Hagos, J. Hardin, Q. Yang, B. Han, and J. Fan, 2018:
631 Structure and evolution of mesoscale convective systems: Sensitivity to cloud microphysics in
632 convection-permitting simulations over the united states. *JAMES*, **10 (7)**, 1470–1494.

633 Feng, Z., and Coauthors, 2021: A global high-resolution mesoscale convective system database
634 using satellite-derived cloud tops, surface precipitation, and tracking. *Journal of Geophysical*
635 *Research: Atmospheres*, **126 (8)**, e2020JD034 202.

636 Fritsch, J., R. Kane, and C. Chelius, 1986: The contribution of mesoscale convective weather
637 systems to the warm-season precipitation in the united states. *Journal of Applied Meteorology*
638 *and Climatology*, **25 (10)**, 1333–1345.

639 Haberlie, A. M., and W. S. Ashley, 2019: A radar-based climatology of mesoscale convective
640 systems in the united states. *J. Climate*, **32 (5)**, 1591–1606.

Held, I. M., R. S. Hemler, and V. Ramaswamy, 1993: Radiative-convective equilibrium with explicit two-dimensional moist convection. *J. Atmos. Sci.*, **50 (23)**, 3909–3927.

Houze, R. A., Jr., 1975: Squall lines observed in the vicinity of the researcher during phase III of GATE. *Preprints, 16th Radar Meteorology Conf., Houston, TX, American Meteorological Society*, 206–209.

Houze, R. A., Jr., 1977: Structure and dynamics of a tropical squall-line system. *Mon. Wea. Rev.*, **105 (12)**, 1540–1567.

Houze, R. A., Jr., 2004: Mesoscale convective systems. *Rev. Geophys.*, **42 (4)**.

Hu, H., Z. Feng, and L. . Ruby Leung, 2021a: Linking flood frequency with mesoscale convective systems in the us. *Geophys. Res. Lett.*, e2021GL092546.

Hu, H., L. R. Leung, and Z. Feng, 2021b: Early warm-season mesoscale convective systems dominate soil moisture–precipitation feedback for summer rainfall in central united states. *Proceedings of the National Academy of Sciences*, **118 (43)**.

Jiang, X., N.-C. Lau, and S. A. Klein, 2006: Role of eastward propagating convection systems in the diurnal cycle and seasonal mean of summertime rainfall over the us great plains. *Geophysical Research Letters*, **33 (19)**.

Knievel, J. C., and R. H. Johnson, 2002: The kinematics of a midlatitude, continental mesoscale convective system and its mesoscale vortex. *Mon. Wea. Rev.*, **130 (7)**, 1749–1770.

LeVeque, R. J., and Coauthors, 2002: *Finite volume methods for hyperbolic problems*, Vol. 31. Cambridge university press.

Li, Y., and R. B. Smith, 2010: The detection and significance of diurnal pressure and potential vorticity anomalies east of the rockies. *J. Atmos. Sci.*, **67 (9)**, 2734–2751.

Lin, G., C. R. Jones, L. R. Leung, Z. Feng, and M. Ovchinnikov, 2022: Mesoscale convective systems in a superparameterized e3sm simulation at high resolution. *Journal of Advances in Modeling Earth Systems*, **14 (1)**, e2021MS002 660.

Maddox, R. A., 1983: Large-scale meteorological conditions associated with midlatitude, mesoscale convective complexes. *Mon. Wea. Rev.*, **111 (7)**, 1475–1493.

Mapes, B. E., 1993: Gregarious tropical convection. *J. Atmos. Sci.*, **50 (13)**, 2026–2037.

Molinari, J., 1993: An overview of cumulus parameterization in mesoscale models. *The representation of cumulus convection in numerical models*, 155–158.

Moncrieff, M., 1978: The dynamical structure of two-dimensional steady convection in constant vertical shear. *Quart. J. Roy. Meteor. Soc.*, **104 (441)**, 543–567.

Moncrieff, M., 1981: A theory of organized steady convection and its transport properties. *Quart. J. Roy. Meteor. Soc.*, **107**, 29–50.

Moncrieff, M., 1985: Steady convection in pressure coordinates. *Quart. J. Roy. Meteor. Soc.*, **111 (469)**, 857–866.

Moncrieff, M., and J. Green, 1972: The propagation and transfer properties of steady convective overturning in shear. *Quart. J. Roy. Meteor. Soc.*, **98 (416)**, 336–352.

Moncrieff, M., and M. Miller, 1976: The dynamics and simulation of tropical cumulonimbus and squall lines. *Quart. J. Roy. Meteor. Soc.*, **102 (432)**, 373–394.

Moncrieff, M. W., 1992: Organized convective systems: Archetypal dynamical models, mass and momentum flux theory, and parametrization. *Quart. J. Roy. Meteor. Soc.*, **118 (507)**, 819–850.

Moncrieff, M. W., 2019: Toward a dynamical foundation for organized convection parameterization in gcms. *Geophys. Res. Lett.*, **46 (23)**, 14 103–14 108.

Moncrieff, M. W., C. Liu, and P. Bogenschutz, 2017: Simulation, modeling, and dynamically based parameterization of organized tropical convection for global climate models. *J. Atmos. Sci.*, **74 (5)**, 1363–1380.

Munich RE, 2016: Topics geo: Natural catastrophes 2015 analyses, assessment, positions.

Pedlosky, J., and Coauthors, 1987: *Geophysical fluid dynamics*, Vol. 710. Springer.

Pietschnig, M., A. L. Swann, F. H. Lambert, and G. K. Vallis, 2021: Response of tropical rainfall to reduced evapotranspiration depends on continental extent. *J. Climate*, **34 (23)**, 9221–9234.

Pinto, J. O., J. A. Grim, and M. Steiner, 2015: Assessment of the high-resolution rapid refresh model's ability to predict mesoscale convective systems using object-based evaluation. *Weather and Forecasting*, **30 (4)**, 892–913.

Pokharel, B., S.-Y. S. Wang, J. Meyer, R. Gillies, and Y.-H. Lin, 2019: Climate of the weakly-forced yet high-impact convective storms throughout the ohio river valley and mid-atlantic united states. *Climate Dyn.*, **52 (9)**, 5709–5721.

Prein, A. F., C. Liu, K. Ikeda, R. Bullock, R. M. Rasmussen, G. J. Holland, and M. Clark, 2017a: Simulating north american mesoscale convective systems with a convection-permitting climate model. *Climate Dyn.*, 1–16.

Prein, A. F., C. Liu, K. Ikeda, S. B. Trier, R. M. Rasmussen, G. J. Holland, and M. P. Clark, 2017b: Increased rainfall volume from future convective storms in the us. *Nature Climate Change*, **7 (12)**, 880–884.

Raymond, D., and H. Jiang, 1990: A theory for long-lived mesoscale convective systems. *J. Atmos. Sci.*, **47 (24)**, 3067–3077.

Romps, D. M., 2014: Rayleigh damping in the free troposphere. *J. Atmos. Sci.*, **71 (2)**, 553–565.

Rotunno, R., J. B. Klemp, and M. L. Weisman, 1988: A theory for strong, long-lived squall lines. *J. Atmos. Sci.*, **45 (3)**, 463–485.

Song, F., Z. Feng, L. R. Leung, B. Pokharel, S.-Y. S. Wang, X. Chen, K. Sakaguchi, and C.-c. Wang, 2021: Crucial roles of eastward propagating environments in the summer mcs initiation over the us great plains. *Journal of Geophysical Research: Atmospheres*, **126 (16)**, e2021JD034 991.

Song, F., L. R. Leung, Z. Feng, X. Chen, and Q. Yang, 2022: Observed and projected changes of large-scale environments conducive to spring mcs initiation over the us great plains. *Geophys. Res. Lett.*, **49 (15)**, e2022GL098 799.

Stensrud, D. J., J.-W. Bao, and T. T. Warner, 2000: Using initial condition and model physics perturbations in short-range ensemble simulations of mesoscale convective systems. *Mon. Wea. Rev.*, **128 (7)**, 2077–2107.

718 Tuttle, J. D., and C. A. Davis, 2013: Modulation of the diurnal cycle of warm-season precipitation
719 by short-wave troughs. *J. Atmos. Sci.*, **70 (6)**, 1710–1726.

720 Wang, S.-Y., T.-C. Chen, and J. Correia, 2011a: Climatology of summer midtropospheric pertur-
721 bations in the us northern plains. part i: Influence on northwest flow severe weather outbreaks.
722 *Climate Dyn.*, **36 (3)**, 793–810.

723 Wang, S.-Y., T.-C. Chen, and E. S. Takle, 2011b: Climatology of summer midtropospheric pertur-
724 bations in the us northern plains. part ii: Large-scale effects of the rocky mountains on genesis.
725 *Climate Dyn.*, **36 (7-8)**, 1221–1237.

726 Weisman, M. L., and R. Rotunno, 2004: "a theory for strong long-lived squall lines" revisited.
727 *Journal of the Atmospheric Sciences*, **61 (4)**, 361–382.

728 Wing, A. A., K. Emanuel, C. E. Holloway, and C. Muller, 2017: Convective self-aggregation
729 in numerical simulations: A review. *Shallow clouds, water vapor, circulation, and climate*
730 *sensitivity*, 1–25.

731 Yang, Q., L. R. Leung, Z. Feng, and X. Chen, in press: Impact of globalwarming on u.s. summertime
732 mesoscale convective systems: A simple lagrangian parcel model perspective. *J. Climate*.

733 Yang, Q., L. R. Leung, Z. Feng, F. Song, and X. Chen, 2021: A simple lagrangian parcel model
734 for the initiation of summertime mesoscale convective systems over the central united states. *J.*
735 *Atmos. Sci.*, **78 (11)**, 3537–3558.

736 Yang, Q., and A. J. Majda, 2017: Upscale impact of mesoscale disturbances of tropical convection
737 on synoptic-scale equatorial waves in two-dimensional flows. *J. Atmos. Sci.*, **74 (9)**, 3099–3120.

738 Yang, Q., and A. J. Majda, 2018: Upscale impact of mesoscale disturbances of tropical convection
739 on convectively coupled kelvin waves. *J. Atmos. Sci.*, **75 (1)**, 85–111.

740 Yang, Q., and A. J. Majda, 2019: Upscale impact of mesoscale disturbances of tropical convection
741 on 2-day waves. *Journal of the Atmospheric Sciences*, **76 (1)**, 171–194.

742 Yang, Q., A. J. Majda, and N. D. Brenowitz, 2019a: Effects of rotation on the multiscale organi-
743 zation of convection in a global 2d cloud-resolving model. *J. Atmos. Sci.*, **76 (11)**, 3669–3696.

744 Yang, Q., A. J. Majda, and M. W. Moncrieff, 2019b: Upscale impact of mesoscale convective
745 systems and its parameterization in an idealized gcm for an MJO analog above the equator. *J.*
746 *Atmos. Sci.*, **76 (3)**, 865–892.

747 Yano, J.-I., and K. Emanuel, 1991: An improved model of the equatorial troposphere and its
748 coupling with the stratosphere. *J. Atmos. Sci.*, **48 (3)**, 377–389.

749 Zhang, M., in press: An analytical model of two-dimensional mesoscale circulation and associated
750 properties across squall lines. *not known*.

751 Zhang, T., W. Lin, Y. Lin, M. Zhang, H. Yu, K. Cao, and W. Xue, 2019: Prediction of tropi-
752 cal cyclone genesis from mesoscale convective systems using machine learning. *Weather and*
753 *Forecasting*, **34 (4)**, 1035–1049.